Journal Name

RSCPublishing

COMMUNICATION

Magnetic nanosensors optimized for rapid and reversible self-assembly

Cite this: DOI: 10.1039/x0xx00000x

Elisenda Rodriguez[a], Victor S. Lelyveld[a], Tatjana Atanasijevic[a], Satoshi Okada[a], and Alan Jasanoff[a]*

Received 00th January 2012,
Accepted 00th January 2012

DOI: 10.1039/x0xx00000x

www.rsc.org/

Magnetic nanoparticle-based sensors for MRI have been accelerated to a timescale of seconds using densely-functionalized particles of small size. Parameters that increase response rates also result in large nuclear magnetic relaxation rate and light scattering changes, allowing signals to be detected almost immediately after changes in calcium concentration.

Nanoscale biosensors are frequently based on the spatial reorganization of nanoparticle conjugates, which can give rise to a variety of optical or magnetic effects. Magnetic sensors involve magnetic nanoparticles (MNPs), which strongly affect the transverse relaxation time (T_2) of water proton spins detected by nuclear magnetic resonance (NMR) spectroscopy or imaging (MRI). MNP conjugates have been engineered to undergo reversible analyte-dependent aggregation,[1,2] where the analyte either reversibly cross-links particles itself or modulates binding between moieties attached to the nanoparticle surfaces. This mechanism has yielded sensors capable of producing R_2 (= $1/T_2$) changes of up to two or threefold.[3] Such changes can be detected at nanoparticle concentrations below 100 μM Fe, making MNP-based sensors an attractive alternative to MRI sensors based on T_1 relaxation or other mechanisms. To date, MNP probes that undergo analyte-dependent assembly have been applied for a variety of in vitro NMR assays[4] and as components of implanted biosensors for *in vivo* imaging.[5]

A serious but previously unaddressed limitation of MNP clustering-based sensors is their slow analyte response rates.[6] Utility of MNP probes is compromised because of the long incubation times required to resolve substantial changes in R_2 and because analyte concentration changes that take place much faster than the sensor response times cannot be detected. R_2 changes initiated by addition of target analytes to MNP aggregation sensors have generally been reported to equilibrate over tens of minutes; this includes MNPs designed to cluster in the presence of glucose,[2] calcium ions,[1] and proteins.[7] By comparison, unimolecular sensors detect analytes with response times on the order of seconds or even milliseconds.[6]

How can MNP aggregation kinetics be accelerated? We used the Smoluchowski aggregation-fragmentation formalism to model the dependence of MNP clustering on the characteristics of binary mixtures of particles assumed to interact via complementary surface-

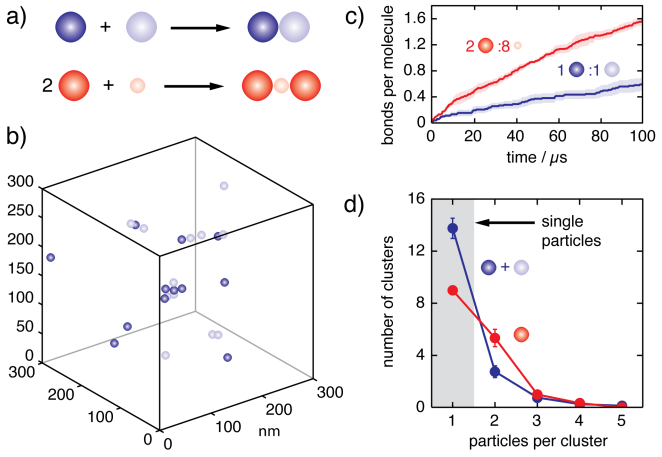

Fig. 1. Increased aggregation rate predicted for asymmetric binary systems. (a) Two scenarios modeled using a Brownian dynamics approach.[8] In the symmetric scenario, which corresponds to prototypical MNP-based calcium sensors,[1] two types of particle (light *vs*. dark blue) could combine by contacting each other and forming a bond; bonds could not be formed between particles of the same type. In the asymmetric scenario implemented experimentally in this paper, particles (dark red) could combine only by being bridged by crosslinking domains (light red) with half the diameter of each particle; crosslinking domains could not aggregate on their own. (b) The configuration of 24 particles following 100 μs of simulation in the symmetric interaction scenario in a 300 nm cubic volume with repeating boundary conditions. (c) Mean number of bonds per molecule (particles and crosslinkers included) over time for simulations of symmetric (blue, n = 8) and asymmetric (red, n = 3) scenarios. Simulations contained equal numbers of particles, with the number of crosslinking domains (light red) in the asymmetric scenario chosen to match the surface area of the particles (dark red). (d) Distribution of cluster sizes following 100 μs simulations depicted in (c). Clusters were classified based on how many particles they contained [light and dark blue or dark red in panel (a)]. The asymmetric scenario (red) produced significantly fewer single-particle species (p = 0.005) and more clustered species (p = 0.0004) than the symmetric scenario (blue).

conjugated binding domains.[6] Optimal rates were predicted when the density of surface functionalization moieties was highest for each MNP. Rates were also predicted to increase for constant MNP volume fraction by using smaller particles. Although the minimum size of interacting nanoparticles is restricted by the physical requirements for effective imaging agents, binary aggregating systems can be constructed by pairing MNPs with smaller crosslinking species.[2] Monte Carlo simulations (Fig. 1) predicted that asymmetric binary systems with similar total particle surface area exhibit roughly twofold faster clustering kinetics than binary systems with two equal particle sizes.

We implemented strategies predicted to enhance MNP sensing kinetics by adapting a prototypical MNP-based calcium ion sensor presented in an earlier study.[1] In this sensor, two different nanoparticle species are prepared separately by conjugation to the calcium-binding protein calmodulin (CaM) and to a peptide (RS20) that binds CaM only in its Ca^{2+}-complexed form. Calcium therefore promotes multivalent binding between complementary particles and reversible clustering with an effective Ca^{2+} dissociation constant of ~1 μM. CaM and RS20 were incorporated into a new MNP platform with reduced particle size, increased protein surface conjugation density, and an asymmetric binary clustering mechanism.

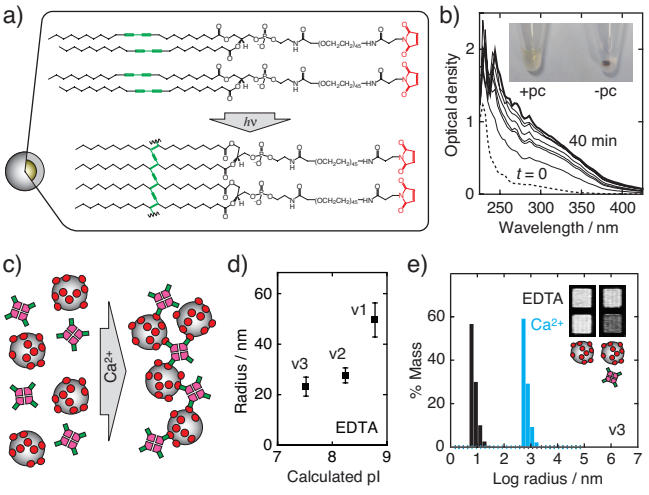

Fig. 2. Optimized nanoparticle aggregation-based sensors. (a) Highly functionalized MNPs are formed by coating iron oxide cores (left) with 23:2 diyne PE-PEG-maleimide. The coating is stabilized by photocrosslinking of the diacetylene moieties (green), which polymerize following irradiation (below arrow). (b) Absorbance spectra taken at time points during irradiation of an MNP sample containing ~1.5 mM Fe; a limiting spectrum (thick line) is approached after 40 minutes. Inset illustrates enhanced stability of photocrosslinked particles (+pc) compared with controls (-pc) in 50% ethanol. The -pc sample is precipitated (brown mark), while the +pc sample remains in suspension. (c) Sensors for Ca^{2+} consist of photocrosslinked particles (pcLCIOs, gray) conjugated to CaM (red) and mixed with a smaller partner consisting of the CaM binding domain RS20 (green) fused to DsRed (magenta). (d) DLS radii of sensor mixtures formed in 250 μM EDTA, consisting of CaM-conjuated nanoparticles and three DsRed-RS20 mutants (v1-v3) with varying estimated isoelectric point (pI), showing effects of electrostatic tuning on Ca^{2+}-independent aggregation. (e) DLS sizes obtained from optimized sensors with a CaM:RS20 ratio of 1:2 in 250 μM EDTA (black) and after addition of 75 μM excess $CaCl_2$ (cyan). Inset: T_2-weighted MRI scans (spin echo *TE/TR* = 150/3125 ms) of samples under Ca^{2+} and EDTA conditions, either with (right) or without (left) addition of DsRed-RS20.v3.

Small, stable, and highly functionalized MNPs were prepared using a novel coating approach (Fig. 2a), based on photocrosslinking of diacetylene-containing lipids.[9] Oleate-stabilized iron oxide cores were mixed with 1,2-bis(10,12-tricosadiynoyl)-*sn*-glycero-3-phosphoethanolamine-*N*-[maleimide(polyethylene glycol)-2000] (23:2 diyne PE-PEG-maleimide), and transferred to aqueous solvent. The resulting lipid-coated particles were subjected to ultraviolet (UV) irradiation at 254 nm for 40 minutes. Progress of the reaction was indicated by UV-visible spectroscopy (Fig. 2b), and the resulting photocrosslinked lipid-coated iron oxide (pcLCIO) nanoparticles were purified by ultracentrifugation to remove micelles and empty liposomes. Particles were characterized by transmission electron microscopy, which indicated electron dense core diameters of 5-10 nm, and by DLS, which indicated a total particle diameter of 16 ± 3 nm (Fig. S1), considerably smaller than commonly used dextran-coated superparamagnetic particles. Enhanced stability of the pcLCIO particles *vs.* uncrosslinked particles was confirmed by comparing their resistance to liposome-disrupting conditions[10] (Fig. 2b, inset), as well as functional tests of calcium sensing properties; these tests revealed that sensors formed from uncrosslinked lipid-coated particles[11] were susceptible to apparent degradation by metal chelators and to spontaneous calcium-independent dissociation of clusters (Fig. S2).

The pcLCIOs were conjugated to CaM via a site-specifically incorporated N-terminal cysteine residue. Protein quantification showed that up to 0.13 μM CaM per 1 μM iron could be conjugated via thiol-maleimide chemistry. This suggests, together with the particle dimensions, that stoichiometries in the range of 10^2-10^3 CaM moieties per pcLCIO particle are attainable, corresponding to functionalization density on the order of one molecule/nm^2, due to the fact that every lipid terminates in a potential conjugation site. MRI assessment of CaM conjugated pcLCIOs indicated a transverse relaxivity of 47 ± 4 (mM Fe)$^{-1}$s^{-1}, measured at 4.7 T.

Asymmetric binary calcium sensors were assembled by pairing CaM-pcLCIOs with a polyvalent engineered protein binding partner, rather than a second nanoparticle species (Fig. 2c). The binding partner was formed by fusing an enhanced version of the 28 kD fluorescent protein DsRed[12] to the N-terminus of RS20 (Fig. 2c). DsRed forms obligate tetramers with a diameter of approximately 6 nm.[13] DsRed-RS20 proteins displayed calcium-dependent clustering in combination with CaM-pcLCIOs, but the aggregation was difficult to reverse except at elevated ionic strength, suggesting that dissociation was hindered by calcium-independent electrostatic interactions. To address this problem, we introduced charge reversal mutations in the DsRed-RS20 construct (Fig. S3) and evaluated reversibility of the corresponding sensors formed by mixing with CaM-pcLCIOs. Sensor properties were progressively improved by mutations K249E, targeting a linker residue between the DsRed and RS20 moieties, and by K188E, at a superficial solvent-exposed residue on DsRed (Fig. 2d). A variant with both substitutions, DsRed-RS20.v3, was used for all further experiments.

Sensors formed from CaM-pcLCIOs and DsRed-RS20.v3 were characterized by DLS and MRI. Sensors initially in EDTA responded to addition of excess $CaCl_2$ by forming clusters ~100 times larger than observed in EDTA (Fig. 2e). Increases in size coincided with decreases in T_2-weighted MRI signal in the presence of the DsRed-RS20 species (Fig. 2e, inset).

Multiple cycles of clustering and declustering were observed by DLS upon successive additions of excess $CaCl_2$ and EDTA (Fig. 3a). In each case, substantial size changes were apparent in seconds for aggregation at high [Ca^{2+}] and within the ~3 s mixing dead time following EDTA addition for disaggregation at low [Ca^{2+}] (Fig. 3a). The effective rate constant for clustering was 0.252 ± 0.004 min^{-1} for sensors containing 50 μM Fe, 12.5 μM DsRed-RS20.v3, and 3.75

μM CaM at 37 °C (Figure S4). We determined a midpoint for calcium responsiveness (EC_{50}) ~1 μM Ca^{2+} for this sensor at steady state, which makes it applicable for the detection of biologically-relevant calcium fluctuations (Fig. S5). The dynamics of sensor clustering varied systematically as a function of CaM levels conjugated to CaM-pcLCIOs (0.006-0.13 μM CaM per μM Fe), with higher levels of CaM per particle resulting in faster and more pronounced aggregation (Fig. 3b), as predicted by the modeling studies.[6] Conjugation density-dependent differences were particularly notable immediately following the mixing dead time, after which clustering was much more pronounced for the most highly functionalized CaM-pcLCIOs (> 10-fold DLS radius increase) than for the least functionalized.

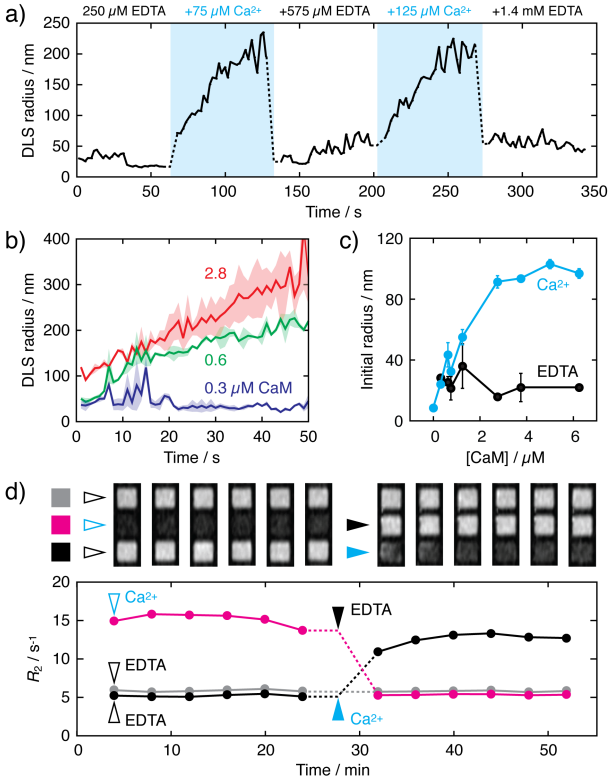

Fig. 3. MNP sensor kinetics. (a) Particle radii as a function of time over two cycles of excess calcium addition and chelation to sensors that contained 50 μM Fe, 1.3 μM CaM, and 12.5 μM DsRed-RS20.v3. Blue indicates periods of high free [Ca^{2+}], and concentrations of excess Ca^{2+} or EDTA present at each time block are indicated. (b) Particle aggregation after 75 μM excess $CaCl_2$ addition is a function of the level of CaM conjugated to the particle surfaces for sensors initially in 250 μM EDTA. Samples each contained 12.5 μM DsRed-RS20.v3 and MNP concentrations corresponding to 50 μM Fe conjugated to 0.3 (dark blue), 0.6 (green), or 2.8 μM (red) CaM. Both initial and final DLS sizes are greater for higher CaM densities. Means (lines) and s.e.m. (shading) for $n = 2$ are shown. (c) The size of aggregates immediately after 75 μM excess calcium addition (blue, dead time ~3 s) increased as a function of CaM conjugation level for samples with 0.3-6.3 μM CaM per 50 μM Fe. Conditions correspond to panels a-b, and EDTA-only controls are shown in black. Error bars show s.e.m. for $n = 2$. (d) MRI visualizes changes in R_2 (graph below) and T_2-weighted image intensity (above; spin echo TE/TR = 160/2000 ms) within minutes of calcium or EDTA addition. Here, sensors were formed with 75 μM Fe, 4.5 μM conjugated CaM, and 12.5 μM DsRed-RS20.v3, initially in 250 μM EDTA. At time $t = 0$ min, the magenta sample received an addition of 75 μM Ca^{2+} and the black and gray samples were maintained in EDTA; initial time points were obtained under these conditions (open arrows). At $t = 28$ minutes, the magenta sample received 575 μM EDTA, the black sample received 75 μM Ca^{2+}, and the gray sample received no addition.

Sensor response dynamics were also analyzed by MRI in microtiter plates. Figure 3d shows images obtained as a function of time during modulation of free Ca^{2+} concentrations. Calcium or EDTA was added five minutes before the first scan (the dead time for sample mixing and positioning in the scanner). An approximately threefold R_2 change is observable in the initial acquisition. R_2 values remain stable for several scans, and are then reversed again within ~5 minutes upon transition from low [Ca^{2+}] to high [Ca^{2+}] or *vice versa*. This is more than an order of magnitude faster than R_2 equilibration times previously reported for MNP aggregation sensors. In particular, for prototypical Ca^{2+} sensors[1] formed without regard for the kinetic optimization principles investigated here, R_2 changes required roughly one hour to equilibrate, despite the use of twofold higher iron concentrations than employed for the experiments of Figure 3d (75 μM Fe).

These results show that robust analyte-dependent responses from nanoparticle aggregation-based probes can be detected within experimental dead times of seconds or minutes by DLS or MRI, respectively, indicating that these types of sensors are appropriate for measurements on biologically and chemically-relevant time scales faster than those previously explored. Examples of potential applications include the rapid *in vivo* detection of metabolites such as glucose, which can change by more than 10% within seconds in brain following stimulation[14] or within minutes following food ingestion.[15] *In vitro* diagnostic modalities based on magnetic[4] or optically-detected[16] nanoparticle aggregation could also be accelerated, allowing measurements to be made at intervals appropriate for rapidly developing clinical conditions such as anaphylaxis or stroke. Finally, although sensors with improved kinetics do not directly address the need for higher affinity detection of some biological targets, we note that accelerating the rate of responses to targets in general confers greater analyte sensitivity, according to mass action principles. The nanosensor design characteristics examined here, in addition to the novel photocrosslinked coating and electrostatic optimization we employed, could therefore find utility in a broad range of applications.

Notes and references

[a] Departments of Biological Engineering, Brain & Cognitive Sciences, and Nuclear Science & Engineering
Massachusetts Institute of Technology, 77 Massachusetts Avenue, Cambridge, Massachusetts 02139, United States.
jasanoff@mit..edu

† **Funding Sources**
ER was supported with the Beatriu Pinos Fellowship from the Government of Catalonia and SO was supported by an Uehara Memorial Foundation postdoctoral fellowship. Additional support was provided by NIH grants DP2-OD2114, R01-DA28299, R01-NS76462, and an MIT Simons Center seed grant to APJ.
Electronic Supplementary Information (ESI) available: [Supplemental Methods and References Sections and Figures S1, S2, S3, S4, and S5]. See DOI: 10.1039/c000000x/

1 T. Atanasijevic, M. Shusteff, P. Fam, A. Jasanoff, *Proc. Natl. Acad. Sci. U S A,* 2006, **103**, 14707-12.

2 E. Y. Sun, R. Weissleder, L. Josephson, *Small,* 2006, **2**, 1144-7.

3 L. Josephson, J. M. Perez, R. Weissleder, *Angew. Chem. Int. Ed. Engl.,* 2001, **40**, 3204-6.

4 H. Shao, C. Min, D. Issadore, M. Liong, T. J. Yoon, R. Weissleder, H. Lee, *Theranostics,* 2012, **2**, 55-65.

5 Y. Ling, T. Pong, C. C. Vassiliou, P. L. Huang, M. J. Cima, *Nat. Biotechnol.,* 2011, **29**, 273-7.

6 M. G. Shapiro, T. Atanasijevic, H. Faas, G. G. Westmeyer, A. Jasanoff, *Magn. Reson. Imaging,* 2006, **24**, 449-62.

7 J. M. Perez, L. Josephson, T. O'Loughlin, D. Hogemann, R. Weissleder, *Nat. Biotechnol.,* 2002, **20**, 816-20.

8 Hütter, M. *J Colloid Interface Sci* **2000**, *231*, 337-50.

9 D. S. Johnston, S. Sanghera, M. Pons, D. Chapman, *Biochim. Biophys. Acta,* 1980, **602**, 57-69.

10 B. M. Shamsai, H. G. Monbouquette, *J. Memb. Sci.,* 1997, **130**, 173-81.

11 N. Nitin, L. E. LaConte, O. Zurkiya, X. Hu, G. Bao, *J. Biol. Inorg. Chem.,* 2004, **9**, 706-12.

12 R. L. Strack, D. E. Strongin, D. Bhattacharyya, W. Tao, A. Berman, H. E. Broxmeyer, R. J. Keenan, B. S. Glick, *Nat. Methods,* 2008, **5**, 955-7.

13 M. A. Wall, M. Socolich, R. Ranganathan, *Nat. Struct. Biol.,* 2000, **7**, 1133-8.

14 E. A. Kiyatkin, M. Lenoir, *J. Neurophysiol.,* 2012, **108**, 1669-84.

15 T. C. Dunn, R. C. Eastman, J. A. Tamada, *Diabetes Care,* 2004, **27**, 2161-5.

16 W. Zhao, M. A. Brook, Y. Li, *Chembiochem,* 2008, **9**, 2363-71.

SUPPORTING INFORMATION

Table of Contents **page**

Figure S1. Size characterization of pcLCIO nanoparticles. (a) Dynamic light scattering (DLS) mass-weighted size histogram showing a mean pcLCIO particle radius of 8.3 ± 1.5 nm. (b) Transmission electron microscopy image of pcLCIOs with intrinsic contrast showing 5-10 nm electron dense cores. Scale bar = 20 nm.

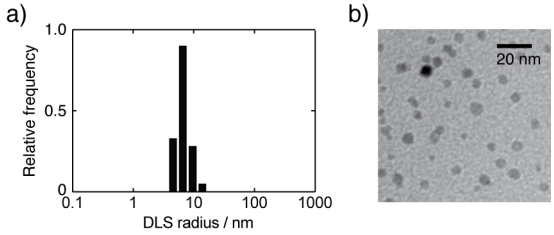

Figure S2. Functional instability of sensors based on uncrosslinked lipid coated iron oxide nanoparticles. (a) Sensors formed with ~16 nm CaM-LCIO and RS20-LCIO nanoparticles aggregated to approximately 200 nm mean cluster size after addition of 500 μM $CaCl_2$ (final concentration), but then appeared to fall apart spontaneously after roughly 15 minutes incubation; no precipitate was visible. (b) 500 μM Ca^{2+} was added to CaM-LCIO/RS20-LCIO mixtures preincubated initially in 100 μM EDTA (black), 1 μM EDTA (gray), or 100 μM EGTA (magenta) for the indicated amounts of time. For preincubation periods ≥ 10 min, little calcium-dependent aggregation could subsequently be observed, suggesting the possibility of exchange or displacement of proteins conjugated to the particle surfaces.

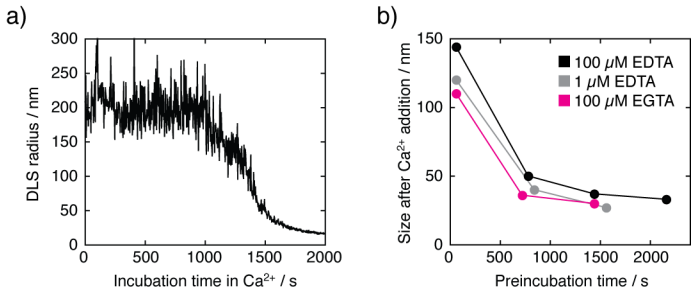

Figure S3. Sequence of DsRed-RS20.v3. Regions corresponding to the hexahistidine tag, DsRed, and RS20 are color coded in blue, magenta, and green, respectively. Locations of the two charge reversal mutations included in this variant and the intermediate DsRed-RS20.v2 variant are highlighted with shaded boxes: K249E (v2 and v3) and K188E (v3 only).

```
  1 MGSSHHHHHH SSGLVPDGSH MASSEDVIKE FMRFKVRMEG SVNGHEFEIE
 51 GEGEGRPYEG TQTAKLKVTK GGPLPFAWDI LSPQFQYGSK VYVKHPADIP
101 DYKKLSFPEG FKWERVMNFE DGGVVTVTQD SSLQDGSFIY KVKFIGVNFP
151 SDGPVMQKKT MGWEASTERL YPRDGVLKGE IHKALKLEDG GHYLVEFKSI
201 YMAKKPVQLP GYYYVDSKLD ITSHNEDYTI VEQYERAEGR HHLFLGSSEG
251 GRRKWQKTGH AVRAIGRLSS S
```

Figure S4. Aggregation rate measured for a sensor containing 50 μM Fe, 12.5 μM DsRed-RS20.v3, and 3.75 μM CaM at 37 °C. A monoexponential curve was fit to the average of two independent DLS traces (red line, s.e.m. indicated by shading). The fit (black line) indicated an effective rate of 0.252 ± 0.004 min^{-1}.

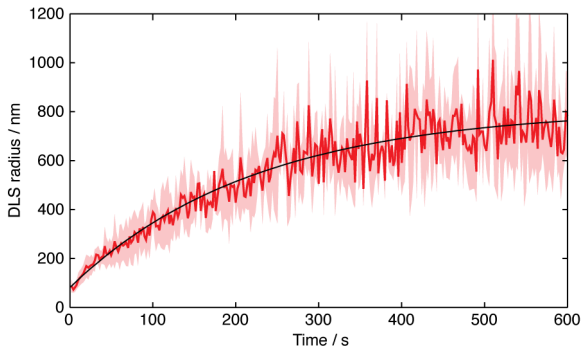

Figure S5. Calcium sensitivity titration curve measured by DLS to determine the EC_{50} of the calcium sensors. DLS was performed at 37 °C after 5 min of mixing the sensors containing 150 µM Fe, 5 µM DsRed-RS20.v3, and 0.75 µM CaM. Solutions with different Ca^{2+} concentrations were formulated using commercial calibration buffers. The calculated EC_{50} for Ca^{2+} was 1.3 µM, as determined by fitting the data to a non-depleting two state model of calcium binding by the sensors.

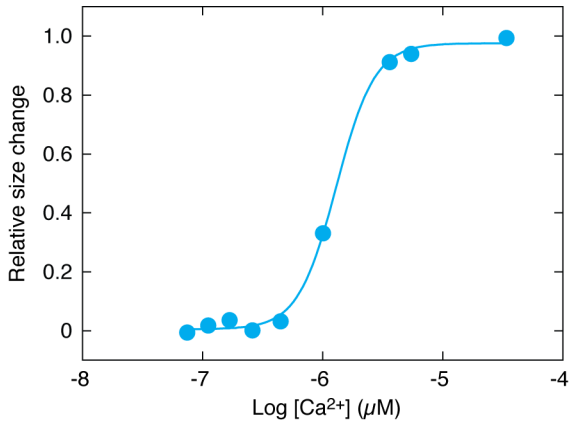

SUPPLEMENTAL METHODS

Supplies. Magnetic iron oxide (Fe_3O_4) nanoparticles with a reported diameter of 5 nm were purchased from Sigma-Aldrich (St. Louis, MO). 1,2-distearoyl-*sn*-glycero-3-phosphoenthanolamine-N-[maleimide(polyethylene glycol)-2000] (DSPE-PEG-maleimide) and 1,2-bis(10,12-tricosadiynoyl)-*sn*-glycero-2-phosphoethanolamine-N-[maleimide(polyethylene glycol)-2000] (23:2 diyne PE-PEG-maleimide) were obtained in lyophilized form from Avanti Polar Lipids (Huntsville, AL), the latter following custom synthesis. Additional chemicals were purchased from Sigma-Aldrich unless otherwise noted.

Lipid coated iron oxide nanoparticle preparation. Uncrosslinked lipid coated iron oxide (LCIO) nanoparticles and photocrosslinked lipid coated iron oxide (pcLCIO) particles were prepared using similar procedures. Solutions of DSPE-PEG-maleimide (LCIOs) or 23:2 diyne DSPE-PEG-maleimide (pcLCIOs) were prepared in $CHCl_3$ (8 mg/mL) and then added to a suspension of 5 nm diameter iron oxide particles initially in toluene. Mixtures were brought to a 1:20 ratio of Fe_3O_4 to lipids (w:w), with a final iron concentration of 0.4 mg/mL. For procedures involving 23:2 diyne DSPE-PEG-maleimide, sample containers were wrapped in aluminum foil in order to protect them from light exposure. Lipid-iron oxide mixtures were dried overnight in a hood. Dried films were resuspended to a concentration of approximately 1.5 mM Fe in 10 mM 4-(2-hydroxyethyl)-1-piperazineethanesulfonic acid (HEPES), pH 7.2 buffer, with 150 mM NaCl. Solutions were filtered though a μMACS magnetic column (Miltenyi Biotec,

Auburn, CA) to remove aggregated species and the flow-through fractions were filtered using 0.2 μm mesh Whatman Anotop syringe filters (GE Healthcare, Piscataway, NJ). Maleimide groups on the surface of the particles were quantified using ultrasensitive thiol and sulfide quantification kit from Life Technologies (Grand Island, NY). Photocrosslinking or control mock-crosslinking procedures were performed by flushing the samples with argon for 15 min and transferring them to a 1 mm quartz cell, followed by irradiation for 40 minutes at 254 nm using an 8 W ultraviolet (UV) lamp placed 10 cm from the cuvette. UV-visible spectroscopy was used to follow the time-course of the photocrosslinking reaction. In order to eliminate empty phospholipid micelles and vesicles, samples were ultracentrifugated for 20 min at 173,000*g*; supernatants were discarded and the particles were resuspended in HEPES buffer.

Nanoparticle iron oxide concentrations were determined using a colorimetric assay based on the iron chelator bathophenanthrolinedisulfonic acid (BPS).[1] Nanoparticle stability was assessed by dynamic light scattering (DLS)-based functional assays and by challenging crosslinked or mock-crosslinked particles at a concentration of 0.5 mM Fe with 50% ethanol for one hour, followed by 5 minutes centrifugation at 3,000*g*. Transmission electron micrographs of pcLCIO samples on carbon grids were obtained using standard methods on a JEOL (Tokyo, Japan) 2010 Advanced High Performance transmission electron microscope.

Protein preparation and conjugation. N-terminally hexahistidine tagged and cysteine modified calmodulin (CaM) from *Xenopus laevis* was recombinantly expressed in *E. coli* and purified using Ni-affinity chromatography as described previously.[2] Purity was

assessed by sodium dodecyl sulfate polyacrylamide gel electrophoresis (SDS-PAGE) following a standard protocol, and protein concentration was measured using the Pierce 660 nm Assay (Thermo Fisher Scientific, Rockford, IL). Purified CaM at concentrations of 21, 42, 85, 170, or 340 μM was added LCIOs or pcLCIOs at 25 mg/mL Fe and incubated for 2 hours at room temperature. Cystamine (11 mg/mL) was added to the particles and incubated for 30 min to quench any free maleimide groups remaining after the CaM conjugation. To remove unconjugated protein, the resulting samples were dialyzed against 1 L of 1 mM HEPES, pH 7.2, 150 mM NaCl for 12 hours, including one buffer change. Finally, samples were filtered using 0.2 μm syringe filters. Final protein concentration conjugated to the nanoparticles was measured using the Pierce 600 nm Assay, and iron concentration was estimated using the BPS assay.

DsRed-RS20 fusion proteins (Supplemental Fig. S3) were constructed by fusing residues the CaM-binding domain of chicken smooth muscle myosin light chain kinase, known as the RS20 peptide (RRKWQKTGHAVRAIGRLSSS), to the C-terminus of an N-terminally polyhistidine tagged fusion of DsRed-Express,[2] an enhanced variant of the red fluorescent protein DsRed. Vectors were based on the commercial expression plasmid pET28a (Novagen, Madison, WI). Site directed mutagenesis within the coding sequence for DsRed-RS20 was performed by polymerase chain reaction and blunt ligation. *E. coli* BL21(DE3)Star cells (Life Technologies) carrying the resulting plasmid were inoculated from an overnight culture at a 1:100 ratio into Luria-Bertani medium supplemented with 100 μg/mL kanamycin, and were grown with vigorous shaking for approximately 3 hours at 37 °C until they reached an OD_{600} ~0.6. Cultures were induced with 1 mM isopropyl β-D-1-thiogalactopyranoside with vigorous shaking for 3 hours at 30 °C followed by gentle

shaking incubation overnight at 4 °C to maximize chromophore maturation. Inclusion bodies were prepared from harvested cell pellets by lysing in BugBuster (Novagen) with lysozyme and benzonase, following the manufacturer's protocol, followed by centrifugation of the resultant crude lysate at 16000 x *g* for 20 minutes. The pelleted inclusion bodies were then solubilized in Pierce Inclusion Body Solubilization Reagent (Thermo Scientific) and batch affinity purified by incubating the solubilized protein with Ni-NTA agarose resin (Qiagen, Valencia CA) under denaturing conditions for 1-2 hours. The resin was then washed in two column volumes of Solubilization Reagent, refolded on column by washing the resin-bound protein in 50 mM sodium phosphate, 300 mM NaCl, 20 mM imidazole, pH 8. Refolded protein was then eluted in an otherwise identical buffer containing 250 mM imidazole. Protein purity was assessed by SDS-PAGE, and protein concentration was determined using the Pierce 660 nm Protein Assay. Isoelectric points (pI values) were estimated using the Scripps Protein Calculator available online.

Light-Scattering Experiments. Dynamic light scattering (DLS) measurements were performed using a DynaPro DLS system (Wyatt Technology, Santa Barbara, CA). Reported particle diameters were obtained from mass-weighted histograms (Fig. 2e and Supplemental Fig. S1) or by extracting single intensity-weighted size parameters from the DLS data (all other figures). Intensity-weighted values were greater than mass-weighted sizes, but could be obtained from fewer time points and were thus most suitable for kinetic measurements. Mixtures of DsRed-RS20 and CaM-LCIO or CaM-pcLCIO variants were formed in 10 mM HEPES, pH 7.2, supplemented with 200 mM NaCl and 250 μM EDTA, except where noted otherwise. Further doses of EDTA or $CaCl_2$ were

added as noted in the text and figure captions. Mixing dead time for DLS kinetic experiments was approximately 3 s. All DLS measurements were performed at 37 °C.

MRI experiments. Samples containing CaM-pcLCIO and DsRed-RS20 variants were formulated as described above, with concentrations of components including EDTA and $CaCl_2$ as noted in the text and figure captions. Aliquots were arrayed into microtiter plates; unused wells were filled with buffer to avoid susceptibility artifacts in imaging. Plates were then placed into a 9 cm inner diameter birdcage coil in a 40-cm-bore Bruker (Billerica, MA) Avance 4.7 T MRI scanner equipped with 12 cm inner diameter triple axis 26 G/cm gradients, and imaging was performed on a 2 mm slice positioned through halfway through the sample height. A T_2-weighted spin echo pulse sequence with multiecho acquisition was used; repetition time (*TR*) was 2 s, and echo time (*TE*) ranged from 10 to 300 ms. Data matrices of 256 x 128 points were acquired with an in-plane resolution of 200 x 400 μm. MRI image time series were obtained after mixing and setup dead time of 4 min, and with an acquisition time of 4 min per scan. MRI experiments were performed at 22 °C.

Aggregation model calculations. The aggregation kinetics of binary nanoparticle sensors were simulated in two scenarios, using a Brownian dynamics approach[1] implemented in Matlab. In the symmetric binary scenario, 24 particles of radius 8 nm, classified as either type A or type B particles (12 of each), were simulated such that each particle type could bind to exclusively to the opposite type. In the asymmetric binary scenario, 24 type A particles were paired with 96 crosslinking domains of a smaller 4 nm

radius (type C), again such that each species could bind exclusively to the opposite type. The ratio of particles to crosslinking domains in the asymmetric scenario was chosen such that the interaction surface area on the two species was equal. Simulations began with particles sited in a uniform random distribution within a 300 nm cubic box with periodic boundary conditions. Positions were adjusted over 20,000 time steps of 5 ns each. At each step, each particle was moved in a random direction by a distance equal to its mean 5 ns diffusion path length, given the diffusion constant calculated by the Stokes-Einstein relation and assuming a viscosity of 1.02 x 10^{-3} Pa-s and temperature of 293 K. A discontinuous bonding probability function was chosen, such that approach of complementary particles to within 1% of the sum of their diameters resulted in a "bond" being formed. Correct bond distances and the absence of overlap among particles were ensured at each diffusion step by also applying an elastic spring force to resolve violations,[1] assuming a constant mass density of 1.4 g/cm^3 for each particle.

Data analysis. MRI scans were reconstructed and analyzed in Matlab (Mathworks, Natick, MA). T_2 relaxation rates (R_2) were determined by exponential fitting to signal amplitudes as a function of echo time, and relaxivity values were determined by linear fitting to a graph of R_2 *vs*. concentration for nanoparticles imaged at 0-320 μM Fe. Further data analysis and figure generation were performed with Matlab, Kaleidagraph (Synergy Software, Reading, PA), and Adobe Creative Suite (Adobe Systems, San Jose, CA).

SUPPLEMENTAL REFERENCES

[1] Tamarit, J.; Irazusta, V.; Moreno-Cermeno, A.; Ros, J. *Anal Biochem* **2006**, *351*, 149-51.

[2] Pfleger, B.F.; Fawzi, N.J.; Keasling, J.D. *Biotechnol Bioeng* **2005**, *92*, 553-8.